Design of a Suspended Manipulator with Aerial Elliptic Winding

Ethan Niddam, Jonathan Dumon, Loïc Cuvillon, Sylvain Durand, Stephane Querry, Ahmad Hably, Jacques Gangloff

Design of a Suspended Manipulator with Aerial Elliptic Winding

Ethan Niddam[1], Jonathan Dumon[2], Loic Cuvillon[1], Sylvain Durand[1], Stephane Querry[3], Ahmad Hably[2], Jacques Gangloff[1]

***Abstract*— Art is one of the oldest forms of human expression, constantly evolving, taking new forms and using new techniques. With their increased accuracy and versatility, robots can be considered as a new class of tools to perform works of art. The STRAD (STReet Art Drone) project aims to perform a 10-meter-high painting on a vertical surface with sub-centimetric precision. To achieve this goal we introduce a new design for an aerial manipulator with elastic suspension capable of moving from one equilibrium position to another using only its thrusters and an elliptic pulley-counterweight system. A feedback linearization control law is implemented to perform fast and accurate winding and unwinding of an elastic cable.**

I. Introduction

Using robotic arms to reproduce human artistic techniques has attracted much attention in recent years. Different approaches have been tried such as observational portrait [1], using a camera as an eye to observe the subject or using visual feedback to control the quality of painting, in grayscale [2] or with colors and multiple layers [3]. The ability to automatically mix colors has been tested in [4] as well as watercolor techniques on a canvas [5]. Drawing on a non-planar canvas has been studied in [6] using first impedance control, then implementing surface estimation to decrease the distortion on the final result [7]. A humanoid robot has been used to perform graffiti art on a wall [8], extending the achievable horizontal workspace by cutting the painting into subsections thanks to the ability of the robot to move horizontally. The TSP-Bot [9] is also based on a mobile setup to perform colorful graffiti by combining stippling and the Traveling Salesman Problem art (TSP art) techniques. However, mobile manipulators and humanoid robots remain grounded, limiting the vertical scale of the artwork achievable by such systems.

Cable-Driven Parallel Robots (CDPRs) and Unmanned Aerial Vehicles (UAVs) are both capable of performing tasks over large horizontal and vertical ranges. The construction CDPR presented in [10] has an almost planar vertical workspace greater than $96\,\mathrm{m}^2$ with centimetric and sub-degree positioning accuracy. It uses 8 winches mounted on 4 crane-like structures secured to the building. A CDPR has been used to replicate an artist movement captured with an optical motion capture device (mocap) to perform spray painting with great precision on a wall [11]. The Paintcopter [12] is a commercial quadcopter holding a custom spray gun controlled by mocap feedback to paint on a non-planar surface. In [13], multiple UAVs are collaborating to paint a large-scale artwork by allocating a part of the whole painting to each robot. The stippling painting technique has been tested with a UAV in [14]. The same authors tried to extend the painting autonomy of their system using a tether in [15]. In all these works, the UAVs are quadcopters. Their underactuation usually impacts the painting task accuracy negatively. CDPRs, on the other hand, are more accurate and have unlimited autonomy. But they are usually more complex to install.

Hybrid systems combining a CDPR with a UAV have recently started to emerge. UAV thrusters have been added to CDPRs to improve the system dynamics, to damp oscillations [16] and to increase the wrench feasible workspace (WFW) [17]. This hybridization yields simpler systems, e.g. using only two cables and two thrusters [18], [19], to accurately control the effector within a large workspace. Simplifying further the CDPR leads to limit the number of cables to the only one required to compensate for gravity, as with the Suspended Aerial Manipulator (SAM) [20] Aerial Manipulators with Elastic Suspension (AMES) have been developed to decouple the slow dynamics of the anchoring point from the fast dynamics of the aerial vehicle (AV) thanks to an elastic linkage [21], [22]. Omniplus AVs allow for generating an omnidirectional wrench by using a limited number of unidirectional thrusters [23]. The SAM and the AMES are both using a 8-thruster Omniplus AV optimized to maximize the reachable workspace (RW) [20], [22]. The equilibrium point (EP) of those manipulators can be controlled by a carrier like a CDPR [24], a crane [20] or a quadcopter [25], [26]. The AVOCADO robot [27] is an underactuated two rotor AV suspended under a quadcopter. It uses a servomotor to wind the cable on an onboard winch in order to change its EP without external actuation.

To further simplify this concept, we propose in this work a new design for an AMES that allows for controlling the EP position using only the onboard thrusters. This is achieved by winding and unwinding an elastic cable around an elliptic pulley only actuated by rotating the AV around its principal axis using its own thrusters. A counterweight is used to generate multiple EP every $360\,\mathrm{deg}$ of the pulley rotation. With our approach it is theoretically possible to extend the reachable workspace infinitely in the vertical direction, the only limit being the cable length and the height of the anchoring point. The existence of multiple EP evenly distributed vertically, allows for minimizing the energy consumption for the painting of a large vertical artwork.

This work was supported by the STRAD project under grant ANR-21-CE33-0021 by the French National Research Agency (ANR).

[1]Strasbourg Univ., CNRS, INSA Strasbourg, ICube UMR 7357, 67000 Strasbourg, France. email: {e.niddam, l.cuvillon, sdurand, jacques.gangloff}@unistra.fr

[2]Univ. Grenoble Alpes, CNRS, Grenoble INP, GIPSA-lab, 38000, Grenoble, France. email: {jonathan.dumon, ahmad.hably}@gipsa-lab.grenoble-inp.fr

[3]Polyvionics, Paris 75015, France. email: stquerry@polyvionics.com

To summarize, we believe that the proposed system is simpler and easier to install than CDPRs, it is more energy-efficient than UAVs and, unlike aerial manipulators, it does not rely on an external carrier like a crane or a motorized winch to move vertically. So, the main contribution of this paper is a novel, low-cost and energy-efficient winding technique based only on aerial actuation for fully actuated suspended aerial manipulators. Furthermore, the usage of this system is not limited to painting. Indeed, this system is compatible with all tasks involving a large vertical surface, such as inspecting or cleaning building facades.

The remainder of the paper is organized as follows. The design of this specific AMES, called the STRAD robot, is presented in Section II. The dynamic model is developed in Section III. The feedback linearization control law is explained in Section IV. Finally, experimental results are presented and discussed in Section V.

II. Design

As stated above, the STRAD robot is an AMES. The elastic cable restoring force helps for compensating for the aerial vehicle's weight which in turn decreases the thrusters energy consumption. Furthermore, the low stiffness of the cable allows the AV for moving freely from the cable upper anchoring point. The lower the stiffness, the larger the reachable workspace of the AV around its equilibrium point (EP) when considering a static anchoring point [22].

A CAD view of the proposed AV design is shown in Fig. 1. It is divided into five main parts:

- A central carbon-fiber tube.
- The painting tool which has not yet been implemented, will be located at the end of the carbon-fiber tube next to the batteries.
- An eight-thruster Omniplus (O^8_+) aerial wrench generator using the optimized propeller orientation found in [20] and [22]. Its plane has been rotated vertically and positioned far from the future painting tool to minimize the risk of potential propeller/wall collision.
- An elliptic pulley mounted on the carbon-fiber tube.
- Two battery packs (one that powers the embedded computer and the other, heavier, that powers the motors) which are offset from the carbon-fiber tube axis to act as a counterweight.

The counterweight is used to compensate for the moment generated by the traction of the cable on the pulley, thus creating a rotational equilibrium. Multiple EPs exist, which are angularly spaced by exactly one turn of the pulley. This feature, which is the main contribution of this work, will be explained in detail in section III-B. Since there is an EP every turn of the pulley, these EPs correspond to equidistant vertical positions. The power needed by the thrusters to regulate the AV at one of its equilibrium position is theoretically null. Thanks to the elastic suspension, moving vertically the AV between to adjacent EPs uses a minimal amount of energy as well as moving the AV horizontally away from the nearest EP.

Most of the main components are clamped on the carbon-fiber tube, to make maintenance easier. The Omniplus frame

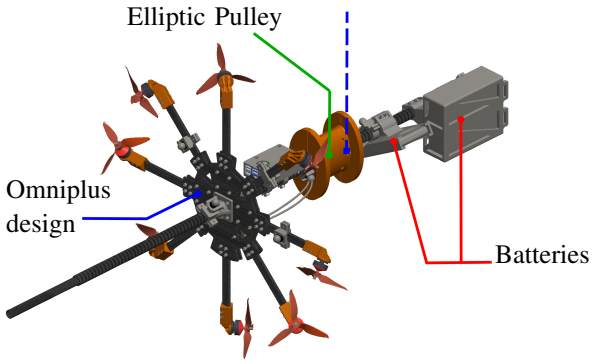

Fig. 1. CAD view of the STRAD robot (dashed blue line = elastic cable)

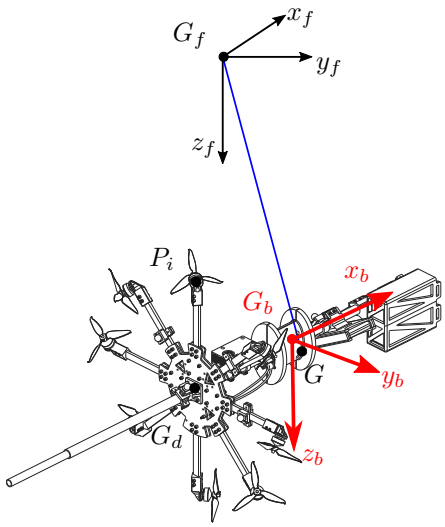

Fig. 2. Frame definition (subscript "f" for "fixed" and "b" for "body")

has been designed like a standard octocopter frame, using two main $3\,\mathrm{mm}$ thick carbon-fiber plates and $6\,\mathrm{mm}$ thick carbon-fiber plates for the arms. The remaining parts have been 3D printed using ABS filaments.

III. Modeling

A. Frames and notations

The inertial frame respects the NED convention, meaning the $\vec{x}_f$ axis is pointing North, the $\vec{y}_f$ axis is pointing East and the $\vec{z}_f$ axis is pointing Down as shown in Fig. 2. We define $\mathcal{R}_f = (G_f, \vec{x}_f, \vec{y}_f, \vec{z}_f)$, the inertial frame with its plane $(\vec{y}_f, \vec{z}_f)$ parallel to the vertical plane of the task, $\mathcal{R}_b = (G_b, \vec{x}_b, \vec{y}_b, \vec{z}_b)$ the body frame and G is the center of mass (CoM) of the AV. The coordinates of G in $\mathcal{R}_b$ are ${}^bG = [0\ g_y\ 0]^T$. The point P_i is the intersection of i^{th} motor axis with the plane of the Omniplus frame. The point G_d is the intersection of a plane perpendicular to the pulley axis containing the points P_i, and the pulley axis. Let us also define $\mathbf{p} = {}^f\mathbf{p}_{b/f} = [x\ y\ z\ ]^T$ as the linear position of G_b expressed in $\mathcal{R}_f$ and $\boldsymbol{\eta}$ as the orientation of $\mathcal{R}_b$ with respect to $\mathcal{R}_f$ using Roll (θ_r), Pitch (θ_p) and Yaw (θ_y) angles (sequential rotations about inertial frame axis $\vec{x}_f$, $\vec{y}_f$ and $\vec{z}_f$). The coordinate z will also be referred to as the altitude in the following. The

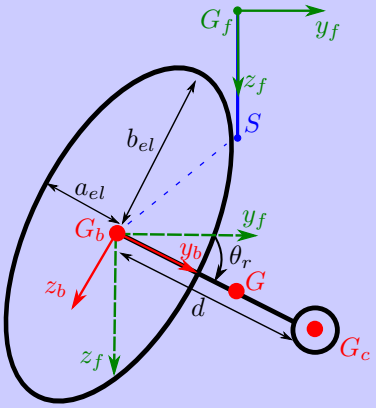

Fig. 3. Planar schematic view of the elliptic pulley and counterweight system at an equilibrium point (G is on the axis $\vec{z}_f$)

symbol $[\cdot]$ is used for the dot product and the symbol $[\times]$ for the cross-product. The notation ${}^a\mathbf{d}$ refers to the coordinates of vector $\mathbf{d}$ in frame $\mathcal{R}_a$. Matrix ${}^b\mathbf{R}_a$ is the rotation matrix between $\mathcal{R}_b$ and $\mathcal{R}_a$ such that ${}^b\mathbf{d} = {}^b\mathbf{R}_a \cdot {}^a\mathbf{d}$.

B. Elliptic Pulley and Counterweight

In this section the choice of an elliptic shape for the pulley is discussed. The counterweight allows for compensating the elastic cable torque around the main axis at the equilibrium position. We suppose that the AV attitude is regulated in such a way that its main axis – the carbon-fiber tube which is also the pulley axis – stays perpendicular to the wall. Since we are studying EPs, we assume that the cable is vertical, which is the only stable configuration of a pendulum. We are looking for stable rotational equilibrium points around the axis of the pulley, so we can simplify the study by modeling the problem in a plane. A planar schematic view of the elliptic pulley and counterweight system is shown in Fig. 3 where G_c and d are respectively the CoM and the offset of the counterweight, a_{el} and b_{el} are respectively the semi-minor and semi-major axis of the ellipse defining the shape of the pulley groove. In the body frame, the CoM position G of the whole AV including the counterweight is:

$$ {}^b\overrightarrow{G_bG} = \begin{bmatrix} 0 \\ g_y = d\frac{m_c}{m} \\ 0 \end{bmatrix} \tag{1} $$

with m_c the mass of the counterweight, m the mass of the whole AV and $d = \|\overrightarrow{G_bG_c}\|$.

The trajectory of a point belonging to an ellipse, while this ellipse is rolling, is known as a roulette [28]. According to [29], the position of the CoM when the elliptic pulley is rolling along the vertical cable is:

$$ \begin{aligned} {}^f\overrightarrow{G_fG} &= {}^f\overrightarrow{G_fG_b} + {}^f\mathbf{R}_b \cdot {}^b\overrightarrow{G_bG} \\ {}^f\overrightarrow{G_fG} &= \begin{bmatrix} 0 \\ -s(\theta_r) \\ z_0 - \int_0^{\theta_r} s(\theta)\, d\theta \end{bmatrix} + {}^f\mathbf{R}_b \cdot {}^b\overrightarrow{G_bG} \end{aligned} \tag{2} $$

where $s(\theta) = \sqrt{(a_{el} \cdot \cos(\theta))^2 + (b_{el} \cdot \sin(\theta))^2}$ and z_0 is the initial value of z. The potential energy is given by $E = -m \cdot g \cdot {}^f\overrightarrow{G_fG}.\vec{z}_f$ with g the gravity acceleration constant, i.e :

$$ E = -m \cdot g \left[z_0 - \int_0^{\theta_r} s(\theta) d\theta + \sin(\theta_r) \cdot g_y \right] \tag{3} $$

A stable equilibrium of a conservative system is characterized by a minimum of its potential energy [30]. Local extrema of the potential energy can be written as the following, according to [28] :

$$ \frac{dE}{d\theta_r} = -m \cdot g \cdot \frac{d^f\overrightarrow{G_fG}.\vec{z}_f}{d\theta_r} = -m \cdot g \cdot {}^f\overrightarrow{G_fG}.\vec{y}_f = 0 \tag{4} $$

Thus, local extrema of potential energy verify equation ${}^f\overrightarrow{G_fG}.\vec{y}_f = 0$. Another interpretation of this condition is that a suspended system at equilibrium has its CoM lying on the vertical line passing through the cable anchoring point. From (2), the local extremum condition becomes:

$$ \sqrt{(a_{el} \cdot \cos(\theta_r))^2 + (b_{el} \cdot \sin(\theta_r))^2} - cos(\theta_r) \cdot g_y = 0 $$

The two corresponding equilibriums θ_{e+} and θ_{e-} are:

$$ \theta_{e\pm} = \pm \arccos\left(\frac{b_{el}}{\sqrt{g_y^2 - a_{el}^2 + b_{el}^2}} \right) \pmod{2\pi} \tag{5} $$

with the constraint $g_y \geq a_{el}$. Examining the second derivative of E at the equilibrium points:

$$ \left.\frac{d^2E}{d\theta_r^2}\right|_{\theta_{e\pm}} = \pm\, m \cdot g \left[\frac{\sqrt{g_y^2 - a_{el}^2 + b_{el}^2} \cdot \sqrt{g_y^2 - a_{el}^2}}{g_y} \right] \tag{6} $$

We conclude that θ_{e+} is a stable solution if $g_y > a_{el}$ since (6) should be strictly positive [30]. If $g_y = a_{el}$, the equilibrium $\theta_{e-} = \theta_{e+} = 0$ is not stable according to the non-zero third derivative of E [30]. This yields the final constraint for a stable equilibrium using the definition of g_y in (1):

$$ d > \frac{m}{m_c} \cdot a_{el} \tag{7} $$

C. Benefits of an Elliptic Pulley

To assess the influence of the elliptic shape, let us introduce $k_{el} = \frac{b_{el}}{a_{el}} \geq 1$ ($k_{el} = 1$ corresponds to a circle) and P the perimeter of the pulley. The potential energy has been plotted in Fig. 4 using the parameters of our system ($P = 0.22\,\mathrm{m}$, $m = 3.95\,\mathrm{kg}$, $d = 0.08\,\mathrm{m}$, $m_c = 1.3\,\mathrm{kg}$) and using three pulley shapes with different k_{el}. From this figure we can conclude that for a given P, d, m and m_c, the system has stable EPs for $k_{el} = 2$ and $k_{el} = 5$ around $\theta_r \equiv 25°$ (mod 360) and has no EP for $k_{el} = 1$ corresponding to a circular pulley. The potential well around $\theta_r \equiv 25°$ (mod 360) is deeper for $k_{el} = 5$ than for $k_{el} = 2$ yielding more robust EPs.

Furthermore, given a constant P, a_{el} decreases when k_{el} increases, which means, according to (7), that the minimum battery offset decreases. Thus, using an elliptic pulley ($k_{el} > 1$) instead of a circular one ($k_{el} = 1$) allows for decreasing the

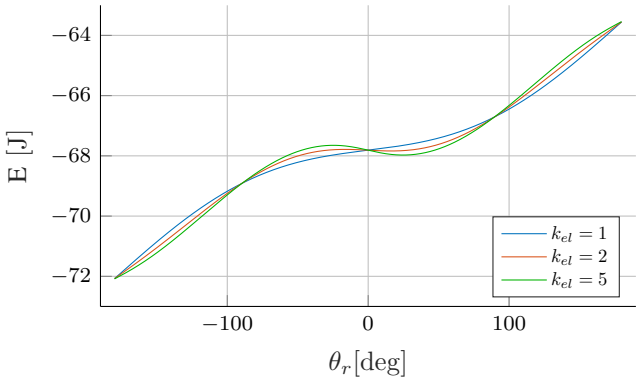

Fig. 4. Potential energy using different semi-major/semi-minor ratio k_{el}

offset d required to generate stable EPs while keeping the same perimeter P. Limiting this offset decreases the required transient winding torque and decreases the unbalanced terms in the body inertia matrix. For example, with the same offset d, the perimeter should have been at least 25% lower to generate an EP when using a circular pulley.

In conclusion, using an elliptic-shaped pulley yields a more compact and balanced AV design with a smaller counterweight offset.

D. Cable Exit Point

In Fig. 3, S is defined as the cable exit point on the pulley. Feedback linearization control technique requires a good model of the system dynamics, so a good knowledge of the cable restoring force application point is required. The cable is supposed to be tangent to the pulley winding surface. By defining the coordinates of ${}^b\overrightarrow{G_bG_f} = [0 \;\; y_{G_f} \;\; z_{G_f}]^T$, the equation of a tangent to an ellipse passing through G_f expressed in $\mathcal{R}_b$ is [31]:

$$\frac{y_b y_{G_f}}{{a_{el}}^2} + \frac{z_b z_{G_f}}{{b_{el}}^2} = 1 \tag{8}$$

Substituting (8) in the ellipse equation $\frac{y_b^2}{a_{el}^2} + \frac{z_b^2}{{b_{el}}^2} = 1$, yields:

$$\left(\frac{{y_{G_f}}^2}{a_{el}^2} + \frac{{z_{G_f}}^2}{b_{el}^2}\right) y_b^2 - 2 y_{G_f} y_b + a_{el}^2 \left(1 - \frac{{z_{G_f}}^2}{b_{el}^2}\right) = 0 \tag{9}$$

which is a quadratic equation giving two solutions. In the case of our design, the coordinate of ${}^b\overrightarrow{G_bS} \times \overrightarrow{SG_f}$ along $\vec{x}_b$ must be negative yielding the following unique solution for S:

$${}^b\overrightarrow{G_bS} = \frac{1}{\epsilon} \begin{bmatrix} 0 \\ y_{G_f} - \gamma \dfrac{a_{el}}{b_{el}} z_{G_f} \\ z_{G_f} + \gamma \dfrac{b_{el}}{a_{el}} y_{G_f} \end{bmatrix} \tag{10}$$

with $\epsilon = \frac{{y_{G_f}}^2}{{a_{el}}^2} + \frac{{z_{G_f}}^2}{{b_{el}}^2}$ and $\gamma = \sqrt{\epsilon - 1}$.

E. Cable Model

The cable stiffness is given by $k = \frac{E_y \cdot A}{l_n}$ where E_y is the Young's modulus of the cable, A its cross-sectional area and l_{n_i} its nominal length – the length at rest of its unwound section – at the i^{th} EP.

Let l_{s_i} be the length of stretched unwound cable section at the i^{th} EP. Using Hooke's law yields:

$$\frac{E_y \cdot A}{l_{n_i}}(l_{s_i} - l_{n_i}) = m \cdot g \implies l_{n_i} = \underbrace{\frac{E_y \cdot A}{m \cdot g + E_y \cdot A}}_{k_e} \cdot l_{s_i} \tag{11}$$

We make the assumption (verified experimentally and in [32]) that the robot is winding stretched cable and that the cable is uniformly stretched within the pulley coils. So we obtain the linear relationship between $l_{s_j} - l_{s_i} = (j-i)P$ and $l_{n_j} - l_{n_i}$, the stretched and unstretched length variations between the i^{th} and the j^{th} EP:

$$l_{n_j} - l_{n_i} = k_e (j - i) P \tag{12}$$

F. External Force and Torque

The gravity force of the system expressed in the inertial frame is:

$${}^f\mathbf{f}_g = m \cdot g \cdot \overrightarrow{z}_f \tag{13}$$

The body frame origin is not at the center of gravity, therefore there is a torque induced by gravity:

$${}^b\mathbf{n}_g = {}^b\overrightarrow{G_bG} \times \left({}^b\mathbf{R}_f \cdot {}^f\mathbf{f}_g\right) \tag{14}$$

where ${}^b\overrightarrow{G_bG}$ is the offset between the body frame origin and the CoM.

Using Hooke's law, the force induced by the elastic cable expressed in the inertial frame is the following:

$${}^f\mathbf{f}_s = k \cdot \left(\|\overrightarrow{SG_f}\| - l_n\right) \cdot \frac{{}^f\overrightarrow{SG_f}}{\|\overrightarrow{SG_f}\|} \tag{15}$$

where k is updated using (12). The torque generated by the elastic cable is given by:

$${}^b\mathbf{n}_s = {}^b\overrightarrow{G_bS} \times \left({}^b\mathbf{R}_f \cdot {}^f\mathbf{f}_s\right) \tag{16}$$

G. Propellers Wrench

In this section, we define the wrench allocation matrix. The force generated by a thruster is given by $F_t = a_f \cdot \omega^2$ where a_f is the aerodynamic lift coefficient and ω is the propeller rotational speed in rad/s. The drag torque generated by a propeller is given by $N_d = a_d \cdot \omega^2$ where a_d is the aerodynamic drag coefficient.

Let us define ${}^b\mathbf{W}$, the wrench matrix giving the relationship between the squared propeller rotational speed and the global aerial wrench applied to AV expressed in the body frame:

$${}^b\mathbf{W} = \begin{bmatrix} \dots & a_f \cdot {}^b\overrightarrow{F_i} & \dots \\ \dots & a_f \cdot ({}^b\overrightarrow{G_bP_i} \times {}^b\overrightarrow{F_i}) + k_{pi} a_d \cdot {}^b\overrightarrow{F_i} & \dots \end{bmatrix} \tag{17}$$

where ${}^b\overrightarrow{F_i}$ is the normalized vector of the i^{th} propeller thrust, ${}^b\overrightarrow{G_bP_i}$ is the position of the i^{th} thruster in body frame and $k_{pi} = \{1, -1\}$ depends on the pitch of the propeller (clockwise or counterclockwise).

The resulting aerial wrench expressed in the body frame is given by:

$$\boldsymbol{\tau}_u = \begin{bmatrix} {}^b\mathbf{f}_u \\ {}^b\mathbf{n}_u \end{bmatrix} = {}^b\mathbf{W} \cdot \mathbf{u} \tag{18}$$

where $\mathbf{u}$ is the vector containing the squared propeller velocities.

H. Equation of Motion

Let us define $[G]^\times$ and $[\omega]^\times$ as skew-symmetric cross product matrices of ${}^b\overrightarrow{G_bG}$ and ${}^b\boldsymbol{\omega}_{b/f}$ respectively with ${}^b\boldsymbol{\omega}_{b/f}$ the AV rotational velocity vector expressed in the body frame. Let's also define $\mathbf{I}_b = (\mathbf{I}_g - m[G]^\times[G]^\times)$, the inertia matrix of the AV in the body frame obtained from the inertia matrix $\mathbf{I}_g$ expressed at the CoM of the AV. We also define ${}^b\mathbf{W}_e$ as the external wrench vector expressed in the body frame:

$$ {}^b\mathbf{W}_e = \begin{bmatrix} {}^b\mathbf{R}_f \cdot \left({}^f\mathbf{f}_g + {}^f\mathbf{f}_s \right) \\ {}^b\mathbf{n}_g + {}^b\mathbf{n}_s \end{bmatrix} \tag{19} $$

Using Newton Euler equations [33], the equation of the AV motion written in the body frame becomes:

$$ \begin{bmatrix} m\mathbf{I}_3 & -m[G]^\times \\ m[G]^\times & \mathbf{I}_b \end{bmatrix} \cdot \begin{bmatrix} {}^b\ddot{\mathbf{p}}_{b/f} \\ {}^b\dot{\boldsymbol{\omega}}_{b/f} \end{bmatrix} + \begin{bmatrix} m[\omega]^\times[\omega]^\times \cdot {}^b\overrightarrow{G_bG} \\ [\omega]^\times \mathbf{I}_b \cdot {}^b\boldsymbol{\omega}_{b/f} \end{bmatrix} = {}^b\mathbf{W}_e + {}^b\mathbf{W} \cdot \mathbf{u} \tag{20} $$

IV. Control Law

A. Definitions

Let $\mathbf{X} = [{}^f\mathbf{p}_{b/f}^T \quad \boldsymbol{\eta}_{b/f}^T]^T$ be the AV pose vector with respect to the inertial frame. Vector $\mathbf{u}$ contains the squared rotational speed of each thruster and $\boldsymbol{\tau}_u = {}^b\mathbf{W} \cdot \mathbf{u}$ is the aerial wrench generated by the control law to follow $\mathbf{X}_{ref} = [{}^f\mathbf{p}_{ref}^T \quad \boldsymbol{\eta}_{ref}^T]^T$, where $\mathbf{p}_{ref}$ is the position reference and $\boldsymbol{\eta}_{ref}$ is the attitude reference.

B. Allocation

In the seminal work [23], an O_+^8 design guarantees that:

$$ \forall \boldsymbol{\tau} \in \mathbb{R}^6 \quad \exists \mathbf{u} \geq 0 \ \text{ s.t. } \ {}^b\mathbf{W} \cdot \mathbf{u} = \boldsymbol{\tau}_u \tag{21} $$

Thus:

$$ \mathbf{u} = {}^b\mathbf{W}^+ \cdot \boldsymbol{\tau}_u + \mathbf{u}_{null} \tag{22} $$

where ${}^b\mathbf{W}^+$ is the Moore-Penrose inverse of ${}^b\mathbf{W}$, and $\mathbf{u}_{null}$ belongs to the null space of ${}^b\mathbf{W}$.

Our thrusters are in a balanced O_+^8 configuration, meaning that $\mathbf{1}_8$ (i.e. the 8×1 vector containing only ones) belongs to the wrench matrix null space. As in [22], the vector $\mathbf{u}_{null} = \lambda \cdot \mathbf{1_8}$ is chosen with the scalar $\lambda > 0 \in \mathbb{R}$ to ensure a positive thrust on each thruster.

C. Feedback Linearization

Let us define the Jacobian matrix ${}^b\mathbf{S}$ such that ${}^b\boldsymbol{\omega}_{b/f} = {}^b\mathbf{S} \cdot \dot{\boldsymbol{\eta}}_{b/f}$ with:

$$ {}^b\mathbf{S} = \begin{pmatrix} 1 & 0 & -\sin(\theta_p) \\ 0 & \cos(\theta_r) & \sin(\theta_r)\cos(\theta_p) \\ 0 & -\sin(\theta_r) & \cos(\theta_r)\cos(\theta_p) \end{pmatrix} \tag{23} $$

The time derivative of ${}^b\boldsymbol{\omega}_{b/f}$ is given by:

$$ {}^b\dot{\boldsymbol{\omega}}_{b/f} = {}^b\dot{\mathbf{S}} \cdot \dot{\boldsymbol{\eta}}_{b/f} + {}^b\mathbf{S} \cdot \ddot{\boldsymbol{\eta}}_{b/f} \tag{24} $$

Injecting ${}^b\dot{\boldsymbol{\omega}}_{b/f}$ in equation (20) and factoring the acceleration $\ddot{\mathbf{X}}$ yields:

$$ \underbrace{\begin{bmatrix} m{}^b\mathbf{R}_f & -m([G]^\times){}^b\mathbf{S} \\ m([G]^\times){}^b\mathbf{R}_f & \mathbf{I}_b{}^b\mathbf{S} \end{bmatrix}}_{\mathbf{M}(\mathbf{X})} \cdot \underbrace{\begin{bmatrix} {}^f\ddot{\mathbf{p}}_{b/f} \\ \ddot{\boldsymbol{\eta}}_{b/f} \end{bmatrix}}_{\ddot{\mathbf{X}}} + \underbrace{\begin{bmatrix} m[\omega]^\times[\omega]^\times \cdot {}^b\overrightarrow{G_bG} - m[G]^\times \ {}^b\dot{\mathbf{S}} \cdot \dot{\boldsymbol{\eta}}_{b/f} \\ [\omega]^\times \mathbf{I}_b \cdot {}^b\mathbf{S} \cdot \dot{\boldsymbol{\eta}}_{b/f} + \mathbf{I}_b \ {}^b\dot{\mathbf{S}} \cdot \dot{\boldsymbol{\eta}}_{b/f} \end{bmatrix}}_{\mathbf{C}(\mathbf{X},\dot{\mathbf{X}})} = {}^b\mathbf{W}_e + {}^b\mathbf{W} \cdot \mathbf{u} \tag{25} $$

The errors are defined in the inertial frame as:

$$ \mathbf{e} = \mathbf{X}_{ref} - \mathbf{X}, \quad \dot{\mathbf{e}} = \dot{\mathbf{X}}_{ref} - \dot{\mathbf{X}} \tag{26} $$

Let us define the control input $\mathbf{u}$ as:

$$ \hat{\mathbf{M}}(\mathbf{X}) \left(\ddot{\mathbf{X}}_{ref} + \mathbf{K}_p\mathbf{e} + \mathbf{K}_i \int \mathbf{e}dt + \mathbf{K}_d\dot{\mathbf{e}} \right) + \hat{\mathbf{C}}(\mathbf{X},\dot{\mathbf{X}}) - {}^b\hat{\mathbf{W}}_e = {}^b\mathbf{W} \cdot \mathbf{u} \tag{27} $$

where $\hat{\mathbf{M}}(\mathbf{X})$, $\hat{\mathbf{C}}$ and ${}^b\hat{\mathbf{W}}_e$ are estimated values of respectively $\mathbf{M}(\mathbf{X})$, $\mathbf{C}$ and ${}^b\mathbf{W}_e$. Matrices $\mathbf{K}_p$, $\mathbf{K}_i$ and $\mathbf{K}_d$ are constant positive diagonal with respectively k_p, k_i and k_d gains on the diagonal. Thus, substituting $\mathbf{u}$ in the model (25) yields:

$$ \hat{\mathbf{M}}(\mathbf{X}) \left(\ddot{\mathbf{X}}_{ref} + \mathbf{K}_p\mathbf{e} + \mathbf{K}_i \int \mathbf{e}dt + \mathbf{K}_d\dot{\mathbf{e}} \right) + \hat{\mathbf{C}}(\mathbf{X},\dot{\mathbf{X}}) - {}^b\hat{\mathbf{W}}_e = \mathbf{M}(\mathbf{X})\ddot{\mathbf{X}} + \mathbf{C}(\mathbf{X},\dot{\mathbf{X}}) - {}^b\mathbf{W}_e + \mathbf{p}(t) \tag{28} $$

where $\mathbf{p}(t)$ is a wrench disturbance.

If we suppose that $\hat{\mathbf{M}}(\mathbf{X})$, $\hat{\mathbf{C}}$ and ${}^b\hat{\mathbf{W}}_e$ are perfectly estimated, then:

$$ \ddot{\mathbf{e}} + \mathbf{K}_p\mathbf{e} + \mathbf{K}_i \int \mathbf{e}dt + \mathbf{K}_d\dot{\mathbf{e}} = \mathbf{p}(t) \tag{29} $$

The Laplace transform of this equation yields:

$$ s^2\mathbf{E}(s) + \mathbf{K}_p\mathbf{E}(s) + \mathbf{K}_i\frac{1}{s}\mathbf{E}(s) + \mathbf{K}_d s\mathbf{E}(s) = \mathbf{P}(s) \tag{30} $$

where $\mathbf{E}(s)$ and $\mathbf{P}(s)$ are the Laplace transforms of $\mathbf{e}(t)$ and $\mathbf{p}(t)$ respectively. The transfer function of the error is:

$$ \mathbf{E}(s) = \frac{s}{s^3 + k_d s^2 + k_p s + ki}\mathbf{P}(s) \tag{31} $$

where k_p, k_i and k_d are supposed to be the same positive tuning gains used on each degree of freedom (DoF). This transfer function can be stabilized by an appropriate tuning of k_p, k_i and k_d.

V. Experiments

A. Experimental Setup

A prototype has been developed as shown in the video associated with this article[1]. A $1\,\mathrm{m}$ long carbon tube is used as the main axis, the O_+^8 frame is attached at $0.6\,\mathrm{m}$ from the end of the carbon tube.

[1] https://youtu.be/fZkru3tZsYo

TABLE I

MODEL PARAMETERS

Parameter	Description	Value
$E_y \cdot A$	Young's modulus $\times$ section	64.3 N
k_e	Constant of elongation	0.624
m	Systems mass	3.95 kg
g_y	CoM offset	26 mm
z_0	Initial altitude	2.1 m
a_f	Lift coefficient	$1.724\text{E}{-6}\,\text{N s}^2/\text{rad}^2$
a_d	Drag coefficient	$1.5\text{E}{-8}\,\text{Nm s}^2/\text{rad}^2$
a_{el}	Semi-minor axis	0.023 m
b_{el}	Semi-major axis	0.045 m
d_{dtb}	Distance from G_d to G_b	0.28 m
r_d	Radius of the O^8_+ frame	0.25 m
d_{ec}	Diameter of the cable	0.006 m
K_p	Proportionnal gains	[65 60 30 65 60 60]
K_i	Integral gains	[100 110 80 130 110 80]
K_d	Derivative gains	[14 14 14 18 14 14]

The elastic cable (Bungee Cord 6mm $\times$ 10m, Abma Cord) is wound around a 3D-printed elliptic pulley. In the initial state shown in the picture, the AV is at the equilibrium point corresponding to the first turn of cable around the pulley.

The Cartesian position of the AV is provided by a mocap system (Vicon Bonita) running at 200Hz. An on-board inertial measurement unit (Xsens MTi-8) running at 100Hz is used for attitude and angular velocity feedback.

The model parameters are summed up in Tab. I. All the parameters in this table have been obtained experimentally, using a load cell to identify the lift and drag coefficients. The inertia matrix at the center of the body frame (G_b in Fig. 2) is computed numerically on a computer-aided design software (PTC CREO Parametric). We measured the masses of the main components directly (including the electric wiring) to parameterize this computation in order to obtain the best accuracy for the inertia matrix (in kgm^2):

$$\mathbf{I}_b = 10^{-3} \begin{pmatrix} 44.003 & -23.699 & -0.0238 \\ -23.699 & 257.490 & -0.596 \\ -0.0238 & -0.596 & 264.248 \end{pmatrix} \quad (32)$$

Note that the inertia matrix (32) is not diagonal which is mainly caused by the battery offset d.

All the propellers have the same counterclockwise (CCW) pitch (GEMFAN Hurricane 51466V2) in order to help cancel out the drag torque with a balanced O^8_+ structure. Two electronic speed controllers (KM50A Pro Skystars ESCs) drive the 8 direct-current brushless motors (X-NOVA Lightning V2N 2208-1900kv). A flight controller (TMotor CineF7 Velox) runs a modified version of the Betaflight firmware, a well-known and open-source firmware in the first-person-view (FPV) drone pilot community. The modified version of the firmware, developed in our lab, called *Betalink*[2], implements a 8 kHz closed-loop speed regulation of the propeller angular velocity to guarantee an accurate and fast thrust control of each propeller. Two 4500 mA h 6S Lipo batteries power the two ESCs, while a 5 V battery pack (Anker PowerCore Slim 10000) powers the Raspberry Pi 5 used as the main embedded computer.

[2]https://github.com/jacqu/betalink

At the beginning of the experiment, the AV is hung and the cable is manually wound around the pulley to reach the initial equilibrium point. The length l_{s_0} is then estimated using (10). Finally, the nominal length l_{n_0} of the elastic cable is computed with (11): $l_{n_0} = k_e \cdot l_{s_0}$ which gives $k_0 = \frac{E_y \cdot A}{l_{n_0}}$, the initial cable stiffness.

B. Winding and Unwinding Experiments

To assess the performance of the robot during a winding turn (WT) and a unwinding turn (UT), the control law described in section IV is implemented. In these experiments, the robot follows a 6-DoF trajectory parameterized with $\theta_r(t)$ which is a polynomial of the time t. It makes n WT in a given time T, then stabilizes for 10 seconds, and finally follows the same trajectory but reversed, unwinding the cable until it returns to its original position. The trajectory makes a round trip between two EPs. The translational reference is defined as follows:

$$\begin{aligned} x_{ref} &= x_0 + \theta_r(t) \cdot d_{ec} \cdot \frac{1}{2 \cdot \pi} \\ y_{ref} &= y_0 \\ z_{ref} &= z_0 - \int_0^{\theta_r(t)} s(\theta)\, d\theta \end{aligned}$$

for the coordinates $[x\ y\ z\ ]^T$ of G_b in $\mathcal{R}_f$ where x_0, y_0 and z_0 are the initial value of x, y and z. In order to maintain the cable vertical, the reference x_{ref} compensates for the helical winding around the pulley that moves the cable exit point along $\vec{x}_b$ at a rate of one cable diameter d_{ec} per turn. Note that, according to (2), y_{ref} should be equal to $-s(\theta_r(t))$. In practice this yields a small amplitude reference (b_{el} - a_{el} peak-to-peak), fluctuating around y_0, which increases the oscillation of the AV, the tracking error and the power consumption, without any clear benefits aside from keeping the cable vertical. So, regulating this coordinate at a constant y_0 yields a tiny angle of the cable with respect to the vertical that can be easily neglected. The rotational reference for $[\theta_r\ \theta_p\ \theta_y]^T$ is $\theta_{r_{ref}} = \theta_r(t)$, $\theta_{p_{ref}} = 0$ and $\theta_{y_{ref}} = 0$.

The first 6 rows in Tab. II compiles the results of 6 winding experiments with various winding and unwinding times T and various number of turns n. The STRAD robot achieved centimetric position accuracy at the CoM during winding and unwinding, and millimetric accuracy when staying stationary at an equilibrium point. In the most demanding of these tests, the robot achieved a maximum angular velocity of 240 deg/s on average ($n = 2$, $T = 3s$) while keeping the root mean square (RMS) error of the winding angle θ_r below 7.2 deg and below 2.0 deg on the pitch and yaw.

The plots of the trajectory tracking for a WT in two seconds and the corresponding global electric power consumption (combining all the thrusters) are shown in Fig. 5. For better readability of the figure, Cartesian and angular positions are plotted with respect to the initial position at the start of the experiment. So, $\Delta x = x - x_{ref_0}$, $\Delta y = y - y_{ref_0}$, $\cdots$, $\Delta\theta_y = \theta_y - \theta_{y_{ref_0}}$ where x_{ref_0}, y_{ref_0}, $\cdots$, $\theta_{y_{ref_0}}$ are the initial conditions of the reference. The same applies to the reference; for example $\Delta x_{ref} = x_{ref} - x_{ref_0}$. Note that the evolution of the vertical position is inverted in this plot due to the use of the NED convention for the inertial frame. A

TABLE II

RMS ERROR ON EACH COORDINATE

Experiment	Coordinate					
	[mm]			[deg]		
	x	y	z	θ_r	θ_p	θ_y
$n = 1$ turn in $T = 5s$	1.3	1.0	4.4	2.4	0.4	0.5
$n = 1$ turn in $T = 3s$	2.0	3.1	4.6	2.9	0.5	0.6
$n = 1$ turn in $T = 2s$	2.5	5.8	6.7	4.3	0.7	1.1
$n = 1$ turn in $T = 1.5s$	3.6	9.2	9.9	7.2	2.0	1.7
$n = 2$ turn in $T = 10s$	1.2	1.3	5.2	2.5	0.5	0.6
$n = 2$ turn in $T = 3s$	3.5	6.3	16.2	6.7	1.8	2.0
Painting trajectory	2.4	1.1	3.4	0.8	0.2	0.3
Static at an EP	0.2	0.1	0.6	0.3	0.1	0.1

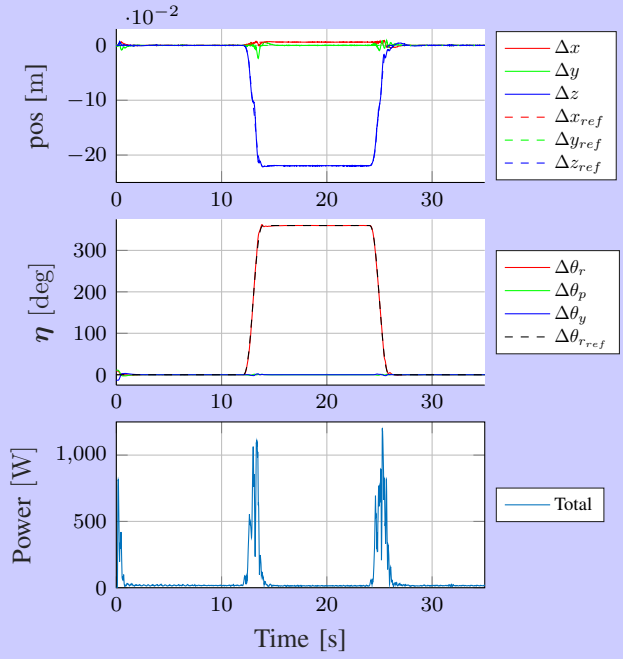

Fig. 5. Trajectory tracking and electric power consumption for a WT and UT during 2s

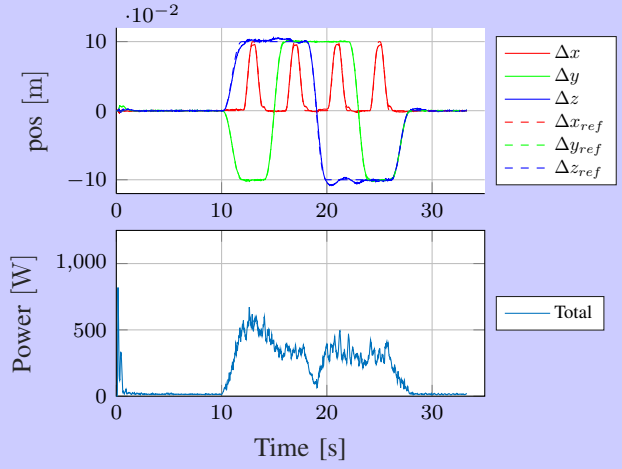

Fig. 6. Trajectory tracking and electric power consumption for painting simulated trajectory

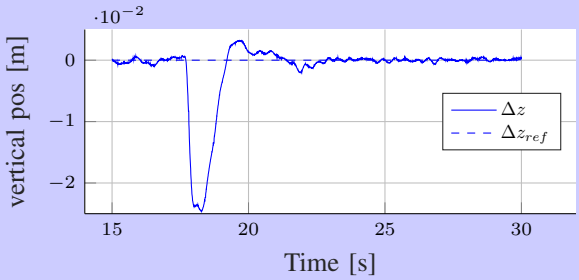

Fig. 7. Rejection of a step disturbance on the vertical position.

video of an experiment where the AMES performs two WT and UT in three seconds is attached to this paper. This plot shows that the power peaks at approximately 1200 W only during the short winding and unwinding phases, while it stays very small (around 17 W) at the EPs.

C. Emulated Painting Experiments

The EPs are evenly scattered vertically at equally spaced discrete positions. But the future painting task requires to make vertical and horizontal translations between these positions. An experiment is carried out where the AV follows during 18 s a vertical 0.2×0.2 m square, making four 0.1 m horizontal translations at each corner, emulating a pointillism dot painting technique. The results of this experiment with the corresponding power consumption are shown in Fig. 6 and in the video attached to this paper. In this experiment, the tracking RMS error stays below 3.5 mm for the translations and below 0.8 deg for the rotations, which is an accuracy compatible with a high-quality fresco. As expected, the average power consumption is significantly higher (see Fig. 6), rising from 14 W at the initial EP to 550 W, at the painting position of lower left corner of the square, which is 0.17 m away from the EP. The length of the cable during this experiment was approximately $l_s = 2$ m, which is a worst-case scenario compared to the 10 m or more length of cable used for large-scale painting. Indeed, the shorter the length, the higher the stiffness and the force needed to travel away from an EP.

D. Disturbance Rejection

Fig. 7 presents the effect of a step disturbance of 5 N on the vertical position regulation. This experiment assesses the effect of outdoor disturbances like the wind or the effect of an uneven winding of the cable on the pulley. This step amplitude can be considered as a worst-case scenario and it yields a transient error of 2.5 cm rejected in less than 1.6 s, which is acceptable.

VI. Conclusion and Future Work

In this paper, a new design for an AMES using an elliptic pulley and a counterweight creating discrete equilibrium points has been introduced. A feedback linearization control law has been implemented and various experiments have been carried out to assess its winding and unwinding performance, as well as the noticeable decrease of the energy need to operate the system. High winding velocities have been achieved while

accurately following the reference trajectory with a WT performed in only 1.5 s. The system has no additional actuators dedicated to the winding, yielding a frugal design. Millimetric accuracy has been achieved during pose regulation. With these features, this AMES is suited to a large set of tasks on a large workspace while being fast, accurate, easy to deploy with its single anchoring point and with a good battery performance.

Future work will focus on the use of other sensors to estimate the position of the robot in order to simplify further the system by removing the mocap device which is not suited to outdoor experiments.

REFERENCES

[1] P. Tresset and F. Fol Leymarie, "Portrait drawing by Paul the robot," *Computers & Graphics*, vol. 37, no. 5, pp. 348–363, Aug. 2013.

[2] T. Lindemeier, S. Pirk, and O. Deussen, "Image stylization with a painting machine using semantic hints," *Computers & Graphics*, vol. 37, no. 5, pp. 293–301, Aug. 2013.

[3] T. Lindemeier, J. Metzner, L. Pollak, and O. Deussen, "Hardware-Based Non-Photorealistic Rendering Using a Painting Robot," *Computer Graphics Forum*, vol. 34, no. 2, pp. 311–323, May 2015.

[4] R. C. Luo, M.-J. Hong, and P.-C. Chung, "Robot Artist for colorful picture painting with visual control system," in *2016 IEEE/RSJ International Conference on Intelligent Robots and Systems (IROS)*. Daejeon, South Korea: IEEE, Oct. 2016, pp. 2998–3003.

[5] L. Scalera, S. Seriani, A. Gasparetto, and P. Gallina, "Watercolour Robotic Painting: a Novel Automatic System for Artistic Rendering," *Journal of Intelligent & Robotic Systems*, vol. 95, no. 3-4, pp. 871–886, Sept. 2019.

[6] D. Song, T. Lee, and Y. J. Kim, "Artistic Pen Drawing on an Arbitrary Surface Using an Impedance-Controlled Robot," in *2018 IEEE International Conference on Robotics and Automation (ICRA)*. Brisbane, QLD: IEEE, May 2018, pp. 4085–4090.

[7] D. Song and Y. J. Kim, "Distortion-free Robotic Surface-drawing using Conformal Mapping," in *2019 International Conference on Robotics and Automation (ICRA)*. Montreal, QC, Canada: IEEE, May 2019, pp. 627–633.

[8] Y. Jun, G. Jang, B.-K. Cho, J. Trubatch, I. Kim, S.-D. Seo, and P. Y. Oh, "A humanoid doing an artistic work - graffiti on the wall," in *2016 IEEE/RSJ International Conference on Intelligent Robots and Systems (IROS)*. Daejeon, South Korea: IEEE, Oct. 2016, pp. 1538–1543.

[9] D. Song, E. Lim, J. Park, M. Jung, and Y. J. Kim, "TSP-Bot: Robotic TSP Pen Art using High-DoF Manipulators," Sept. 2023, arXiv:2210.07592 [cs]. [Online]. Available: http://arxiv.org/abs/2210.07592

[10] K. Iturralde *et al.*, "Cable-driven parallel robot for curtain wall module installation," *Automation in Construction*, vol. 138, p. 104235, June 2022.

[11] G. Chen, S. Baek, J.-D. Florez, W. Qian, S.-W. Leigh, S. Hutchinson, and F. Dellaert, "GTGraffiti: Spray Painting Graffiti Art from Human Painting Motions with a Cable Driven Parallel Robot," in *2022 International Conference on Robotics and Automation (ICRA)*. Philadelphia, PA, USA: IEEE, May 2022, pp. 4065–4072.

[12] A. S. Vempati, M. Kamel, N. Stilinovic, Q. Zhang, D. Reusser, I. Sa, J. Nieto, R. Siegwart, and P. Beardsley, "PaintCopter: An Autonomous UAV for Spray Painting on Three-Dimensional Surfaces," *IEEE Robotics and Automation Letters*, vol. 3, no. 4, pp. 2862–2869, Oct. 2018.

[13] A. Uryasheva, M. Kulbeda, N. Rodichenko, and D. Tsetserukou, "DroneGraffiti: autonomous multi-UAV spray painting," in *ACM SIGGRAPH 2019 Studio*. Los Angeles California: ACM, July 2019, pp. 1–2.

[14] B. Galea, E. Kia, N. Aird, and P. G. Kry, "Stippling with Aerial Robots," *Computational Aesthetics*, p. 10 pages, 2016, artwork Size: 10 pages ISBN: 9783038680000 Publisher: The Eurographics Association.

[15] B. Galea and P. G. Kry, "Tethered flight control of a small quadrotor robot for stippling," in *2017 IEEE/RSJ International Conference on Intelligent Robots and Systems (IROS)*. Vancouver, BC: IEEE, Sept. 2017, pp. 1713–1718.

[16] L. Cuvillon, M. A. Perozo, A. Yiğit, S. Durand, and J. Gangloff, "Offset-free nonlinear model predictive control for improving dynamics of cable-driven parallel robots with on-board thrusters," *Mechanism and Machine Theory*, vol. 180, p. 105141, Feb. 2023.

[17] Y. Sun, Y. Guo, C. Song, and D. Lau, "Wrench-feasible workspace-based design of hybrid thruster and cable driven parallel robots," *Mechanism and Machine Theory*, vol. 172, p. 104758, June 2022.

[18] K. Lee, K. Ko, S. Park, H. S. Kim, and T. Seo, "Obstacle-Overcoming and Stabilization Mechanism of a Rope-Riding Mobile Robot on a Façade," *IEEE Robotics and Automation Letters*, vol. 7, no. 2, pp. 1372–1378, Apr. 2022.

[19] S. Yoo, T. Kim, M. Seo, J. Oh, H. S. Kim, and T. Seo, "Position-Tracking Control of Dual-Rope Winch Robot With Rope Slip Compensation," *IEEE/ASME Transactions on Mechatronics*, vol. 26, no. 4, pp. 1754–1762, Aug. 2021.

[20] Y. S. Sarkisov, M. J. Kim, D. Bicego, D. Tsetserukou, C. Ott, A. Franchi, and K. Kondak, "Development of SAM: cable-Suspended Aerial Manipulator," in *2019 International Conference on Robotics and Automation (ICRA)*. Montreal, QC, Canada: IEEE, May 2019, pp. 5323–5329.

[21] A. Yigit, M. A. Perozo, L. Cuvillon, S. Durand, and J. Gangloff, "Novel Omnidirectional Aerial Manipulator With Elastic Suspension: Dynamic Control and Experimental Performance Assessment," *IEEE Robotics and Automation Letters*, vol. 6, no. 2, pp. 612–619, Apr. 2021.

[22] M. A. Perozo, J. Dussine, A. Yigit, L. Cuvillon, S. Durand, and J. Gangloff, "Optimal Design and Control of an Aerial Manipulator with Elastic Suspension Using Unidirectional Thrusters," in *2022 International Conference on Robotics and Automation (ICRA)*. Philadelphia, PA, USA: IEEE, May 2022, pp. 1976–1982.

[23] M. Tognon and A. Franchi, "Omnidirectional Aerial Vehicles With Unidirectional Thrusters: Theory, Optimal Design, and Control," *IEEE Robotics and Automation Letters*, vol. 3, no. 3, pp. 2277–2282, July 2018.

[24] A. Yiğit, L. Cuvillon, M. A. Perozo, S. Durand, and J. Gangloff, "Dynamic Control of a Macro–Mini Aerial Manipulator With Elastic Suspension," *IEEE Transactions on Robotics*, vol. 39, no. 6, pp. 4820–4836, Dec. 2023.

[25] R. Miyazaki, H. Paul, T. Kominami, and K. Shimonomura, "Wire-Suspended Device Control Based on Wireless Communication With Multirotor for Long Reach-Aerial Manipulation," *IEEE Access*, vol. 8, pp. 172 096–172 104, 2020.

[26] R. Miyazaki, W. Matori, T. Kominami, H. Paul, and K. Shimonomura, "Multirotor Long-Reach Aerial Pruning with Wire-Suspended Saber Saw," in *2022 IEEE/RSJ International Conference on Intelligent Robots and Systems (IROS)*. Kyoto, Japan: IEEE, Oct. 2022, pp. 1787–1793.

[27] S. Kirchgeorg, E. Aucone, F. Wenk, and S. Mintchev, "Design, Modeling, and Control of AVOCADO: A Multimodal Aerial-Tethered Robot for Tree Canopy Exploration," *IEEE Transactions on Robotics*, vol. 40, pp. 592–605, 2024.

[28] Ulrich Abel, Linda Beukemann, and Vitaliy Kushnirevych, "Rolling Curves: An Old Proof of the Roulette Lemma," *The American Mathematical Monthly*, vol. 124, no. 8, p. 723, 2017.

[29] J. Lindén, K.-M. Källman, and M. Lindberg, "The rolling elliptical cylinder," *American Journal of Physics*, vol. 89, no. 4, pp. 358–364, Apr. 2021.

[30] F. Beer, P. Cornwell, D. Mazurek, and E. Johnston, *Vector Mechanics for Engineers: Statics and Dynamics*. McGraw-Hill Education, 2010.

[31] D. A. Brannan, M. F. Esplen, and J. J. Gray, *Geometry*, 2nd ed. Cambridge University Press, 2011.

[32] S. Yoo, T. Kim, M. Seo, J. Oh, J. Kim, H. S. Kim, and T. Seo, "Modeling and verification of multi-winding rope winch for facade operation," *Mechanism and Machine Theory*, vol. 155, p. 104105, Jan. 2021.

[33] H. Hahn, *Rigid Body Dynamics of Mechanisms*. Berlin, Heidelberg: Springer Berlin Heidelberg, 2002.